Optical and Near Infrared Monitoring of the Black-Hole X-ray Binary GX 339-4 During 2002-2010

M. M. Buxton, C. D. Bailyn, H. Capelo, and R. Chatterjee

Astronomy Department, Yale University,P.O. Box 208101, New Haven, CT 06520-8101

michelle.buxton@yale.edu

and

Tolga Dinçer and Emrah Kalemci

Sabanci University, Orhanli-Tuzla, Istanbul, 34956, Turkey

and

John A. Tomsick

Space Sciences Laboratory, 7 Gauss Way, University of California, Berkeley, CA, 94720-7450, USA

Received _____; accepted _____

ABSTRACT

We present the optical/infra-red lightcurve of the black hole X-ray binary GX 339-4 collected at the SMARTS 1.3m telescope over the past nine years. During this time, the source has undergone numerous state transitions. We show that the O/IR colors follow two distinct tracks, which reflect the X-ray state of the source. Thus the X-ray behavior can be accurately inferred from O/IR observations alone. We attempt to decompose the O/IR flux into components associated with the companion star, accretion disk, and jet. The complexity of the system, and undersampling of the spectral energy distribution, make an unambiguous decomposition difficult. We urge caution in fitting simple, one-component flux models to the O/IR flux from this source. We have conducted a timing analysis of the light curve for the hard and soft states and find no evidence of a specific timescale within the range of 4-230 days.

Subject headings: binaries: close — black hole physics — infrared: stars —radiation mechanisms: non-thermal — radiation mechanisms: thermal — stars: individual (GX 339-4)

1. Introduction

Observations of X-ray emitting binary stars provide clear evidence for the presence of accreting black holes in some of these systems since dynamical measurements of the mass of the accreting compact object are greater than the maximum mass of a neutron star (Remillard & McClintock 2006 and references therein).

GX 339-4 is unusual among black hole X-ray binaries in that it has not been observed to go into a "quiescent" state during which the flux from the companion star dominates over the flux from the accretion flow. This has complicated efforts to determine the mass and binary parameters of the system (e.g., Buxton & Vennes 2003). However, observations of emission features associated with the irradiated companion star and accretion disk were successful in determining the orbital period and mass function of the source (Hynes et al. 2003) so it is clear that this source does contain a black hole.

While the lack of a quiescent state has complicated studies of the binary parameters of GX 339-4, its continuous accretion has made it a key source for studying the spectral energy distribution and variability of accreting stellar mass black holes (Homan et al. 2005; Gandhi et al. 2008; Maitra et al. 2009; Coriat et al. 2009; Casella et al. 2010; Gandhi et al. 2010, and references therein). In particular, recent work has focused on evidence for the presence of jet emission which, in some circumstances, can be detected across the whole electromagnetic spectrum (Fender 2001; Coriat et al. 2009). Given the strong variability on all observable timescales from this source, truly simultaneous data across many wavelength regimes is required to carry out such studies.

Over the past decade, we have attempted to provide ongoing monitoring of GX 339-4 in optical and near-infrared wavelengths (hereafter O/IR) by observing the source on a nightly basis (weather permitting) with the Small and Moderate Aperture Research Telescope System (SMARTS). Here we present the full light curve through September

2010.[1] In Section 2 we describe our observations; in Section 3 we distinguish two different patterns of O/IR behavior, which are associated with the "soft" and "hard" X-ray states, and investigate variability timescales in each case; in Section 4 we discuss our results and conclusions.

2. Observations and Data Analysis

2.1. Optical and Near-Infrared

O/IR observations of GX 339-4 were taken with the ANDICAM[2] camera (Depoy et al. 2003) on the SMARTS 1.3m telescope (Subasavage et al. 2010). ANDICAM is a dual-channel imager that contains a movable internal mirror in the IR channel which allows dithered images to be taken while a single optical exposure is undertaken. We obtained pairs of images in $V + J$ and $I + H$ filters on a daily or near-daily basis whenever GX 339-4 was available in the night sky. The optical images were single exposures of 300 seconds. The IR images contained 8 dithered images of 30 seconds each. The optical data were bias- and overscan-subtracted, and flat-fielded using the CCDPROC task in IRAF. Infrared data were reduced using in-house IRAF scripts that flat-fielded, sky-subtracted, and combined dithered images.

[1]We will continue to monitor GX 339-4 into the future. Investigators can access data published in this paper and beyond 2010 at http://www.astro.yale.edu/buxton/GX339/, or consult the first or second author for the most recent results.

[2]http://www.astro.yale.edu/smarts/ANDICAM/

2.1.1. Magnitude Determination and Calibration

Uncalibrated O/IR magnitudes were determined using DAOPHOT in IRAF, for which the full-width-half-maximum, sky background and point-spread function were determined separately for every image.

Optical primary standard stars (Landolt 1992) were used to calibrate the optical magnitudes of three comparison stars in the field of GX 339-4. For 210 photometric nights we calculated the calibrated magnitude of each comparison star using photometric zeropoints that were measured from the SMARTS observations of the primary standard stars for each filter, correcting for atmospheric extinction derived from all the standards taken together. The average magnitude of these three comparison stars was then used as a basis for differential photometry with respect to GX 339-4 for all observations. The near-infrared photometry was calibrated using near-infrared primary standard data (Persson et al. 1998) and two comparison stars were used as secondary standards. Only 21 nights of photometric data were used to measure the calibrated magnitudes of the secondary standards as we had limited data on the near-infrared zeropoints.

We show the comparison stars in the optical and near-infrared finding charts shown in Figures 1 and 2. Our calibrated magnitudes of these comparison stars are given in Tables 1 and 2.

2.1.2. Color correction

The $(V - I)$ color of our secondary standards are given in Table 1, and they range from 1.37 - 2.28. For GX 339-4, the majority of $(V - I)$ data vary over the X-ray states between 0.9 and 2.0. The secondary standard colors overlap most of the $(V - I)$ color range exhibited by GX 339-4. We calculated the mean color-term coefficient for the I-band

for 1052 photometric nights between August 2003 and December 2010 to be 0.062 ± 0.048 (1-σ). Therefore, using the average color-term correction for the I-band, the color-term correction for the secondary stars ranges between 0.085 and 0.141 mag.

2.1.3. Photometric Errors

Errors on the V- and I-band differential photometry were obtained by calculating the 1-σ error of 93 stars from 40 nights of data obtained during 2006. Results that deviated more than +/- 3-σ from the mean were rejected, and the mean and σ were recalculated until no more rejections were made. The 1-σ error for each star was plotted against their calibrated magnitude and a 4th-order polynomial was fitted to the resulting distribution. Again we rejected any data that deviated more than +/- 3-σ from the polynomial and recalculated the polynomial fit until no more rejections were made. The same procedure was performed for the IR data, using 44 stars for the J-band and 29 stars for the H-band, from 40 nights in 2006. We used fewer stars than the optical bands because the field of view is smaller and there are fewer stars to choose from.

Figure 3 shows 1-σ errors versus magnitude for the O/IR and the corresponding polynomial fits. Once the polynomial reached a minimum, we extended that constant numerical value to brighter magnitudes. Thus the optical photometric errors are 0.01 mag for $V \leq 17.50$ and $I \leq 16.50$. Infrared photometric errors are 0.02 mag for $J \leq 14.10$ and $H \leq 14.10$.

We also measured the error in calibrating the secondary star magnitudes by calculating the standard error of the mean over the number of photometric nights mentioned above. The photometric calibration errors are as follows: $V_{err} = 0.003$ mag, $I_{err} = 0.004$ mag, $J_{err} = 0.02$ mag, $H_{err} = 0.02$ mag. These values do not account for systematic errors

associated with such effects as the difference in effective filter responses between SMARTS and the standard system. Such systematics are likely to contribute a few hundredths of a magnitude of calibration error. Therefore we take the optical calibration errors to be ≈ 0.02 magnitudes and the IR calibration errors to be ≈ 0.03 magnitudes.

2.2. X-ray Data

The X-ray data from proportional counter array (PCA) onboard the Rossi X-ray Timing Explorer (RXTE) was reduced using HEASOFT V6.7. After the standard data screening, the background corrected count rates are extracted from proportional counter unit 2 in 3 channels corresponding to the energy bands of 2.8-5.2 keV, 5.2-9.8 keV, 9.8-25 keV.

2.3. Light Curve

In Figure 4 we present the O/IR lightcurve of GX 339-4 during 2002-2010, inclusive. Gaps in the data are when the source is behind the Sun. We also present the O/IR magnitudes in Table 3, the full version of which can be accessed online.

There are a number of interesting features of this light curve. GX 339-4 clearly does not follow the pattern of long periods of quiescence punctuated by outbursts with a fast-rise, exponential-decay morphology as is often seen in dwarf novae (e.g. Cannizzo & Mattei 1998) and neutron-star X-ray binaries, such as Aql X-1 (Maitra & Bailyn 2008) and many black hole binaries (Chen, Shrader, & Livio 1997). Rather, the source is continually active with strong variability, featuring rapid rises with a large range of decay times. Of the X-ray binaries, this is most similar to the O/IR behavior of GRS 1915+105, which has not gone back into quiescence after its initial outburst in 1994 (Neil, Bailyn, & Cobb 2007). During

2003 and 2005, GX 339-4 displayed a slowly fading decay interrupted by a rebrightening which subsequently declined back to the extrapolation of the previous decay. This behavior is reminiscent of the "IR flare" events observed during the outbursts of 4U1543-47 (Buxton & Bailyn 2004) and XTE J1550-564 (Jain et al. 2001), except that those sources continued to decay to a quiescent level.

In many cases, the changes seen in the optical bands have smaller amplitudes than those that occur at the same time in the near-infrared bands. Obvious examples occur in 2003 and 2005 during the re-brightening phases. The increase in flux is barely noticeable in the V- or I-bands, but is more obvious in the J- and H-bands. There are also examples of sudden drops in IR flux which are accompanied by more modest changes in the optical (Bailyn & Ferrara 2004). This is contrary to what is expected if the O/IR flux originates solely from a thermal source, such as an accretion disk. Disk instabilities (Cannizzo, Chen, & Livio 1995; Lasota 2001) and irradiation models (Dubus et al. 1999; Dubus, Hameury, & Lasota 2001) generally attribute variability to changes in temperature of the accretion disk. In such cases, high luminosity should be correlated with blue color. However, this basic relationship clearly does not hold for GX 339-4, which suggests that a non-thermal emission component is often dominant. It is, therefore, desirable to study the spectral energy distribution (SED) to ascertain what flux sources are present and how they vary and contribute to the overall flux during these changes in the light curve. We present our SED in Sections 3.1 and 3.2.

2.4. Determination of O/IR Flux

To obtain fluxes appropriate for comparing with observations in other wavelength regimes requires two steps. First, the magnitudes must be dereddened so that they are not affected by absorption along the line of sight; second, the dereddened magnitudes must be

converted to flux units.

We have checked our flux calibration method by obtaining observations of optical spectrophotometric standards (LTT 3218, LTT 4816, EG 131, EG 274) and comparing our fluxes to those observed by Hamuy et al. (1992) and Hamuy et al. (1994). Observations were obtained in B, V, R, and I-bands and our magnitudes were converted into fluxes using the method outlined above. We compared the photometric fluxes to the flux calibrated spectrum over the relevant bandpass, and found no deviations larger than 0.05 dex, or 10% of a given flux.

The O/IR magnitudes were dereddened using $A_V = 3.7 \pm 0.3$ (Zdziarski et al. 1998) and the extinction law of Cardelli, Clayton, & Mathis (1989). The errors on the dereddened magnitudes are dominated by the error in A_V, and are as follows: $V_{err} = 0.3$ mag, $I_{err} = 0.1$ mag, $J_{err} = 0.1$ mag, $H_{err} = 0.1$ mag. Therefore, adding the photometric and interstellar redenning errors in quadrature give the following total errors on dereddened magnitudes:$V_{err} = 0.30$ mag, $I_{err} = 0.10$ mag, $J_{err} = 0.10$ mag, $H_{err} = 0.10$ mag.

To convert the dereddened magnitudes to flux (in units of Jy) we used the following zeropoint fluxes (where the zeropoint flux of a given filter is that corresponding to zero magnitude): $V_0 = 3636$ Jy, $I_0 = 2416$ Jy (Bessell, Castelli, & Plez 1998), $J_0 = 1670$ Jy, $H_0 = 980$ Jy (Frogel et al. 1978; Elias et al. 1982). The dereddened fluxes of GX 339-4 for each waveband are given in Table 3.

3. O/IR States in GX 339-4

Coriat et al. (2009) described the correlations between the X-ray and O/IR fluxes in GX 339-4 in which a clear delineation of data is seen between the hard, soft, and intermediate X-ray states. Here we investigate correlations within the O/IR and show how

this relates to the X-ray behavior.

In Figure 5 we plot the V-band magnitudes against I-, J-, and H-band magnitudes. In each plot there are clearly two separate branches. The upper branches become redder with increasing brightness (except for V vs. I which is approximately achromatic) while the lower branches become bluer with increasing brightness. The color vs. brightness trends suggest that the upper branches represent a state in which the O/IR is dominated by non-thermal emission while the lower branch could represent a thermal component. This suggests that at least while it is in the upper branch, the O/IR flux contains components associated directly with the inner accretion flow, in addition to whatever flux is produced directly by the outer accretion disk and the (much fainter) companion star. This behavior could already be inferred from the results of Coriat et al. (2009), who explored the relationships between O/IR flux and X-ray flux and ascertained that the upper branch corresponds to the "hard" X-ray state, and the lower branch to the "soft" state. Figure 5 makes it clear that these accretion states are reflected in the O/IR behavior without reference to any other wavelength regime.

We confirm the association between the O/IR upper and lower branches and the X-ray hard and soft state as follows. First, we defined the "soft" and "hard" X-ray states using the RXTE PCA hardness ratio (HR) data (where HR is the ratio of fluxes in the bands (9.8-25 keV)/(2.8-5.2 keV)). The entire GX 339-4 RXTE dataset was analyzed to obtain fluxes and hardness ratios. The beginning and end of outbursts in the hard state were determined using the light curve and setting a threshold of 10 cts/s/PCU. Then we created spectra and power density spectra in the 3-25 keV band for all observations with good time intervals exceeding 1 ks while the count rate increased. We stopped the analysis when significant changes were observed either in the X-ray spectra or the power spectra indicating a transition to an intermediate state. For all these observations, the spectral

index was less than 1.75, and the power spectrum was dominated by broad Lorentzians with mean rms amplitudes greater than 25%. The hardness ratio threshold including all observations was 0.6, however, for some outbursts the threshold can go up to 0.75. When categorizing the O/IR into soft and hard states, we defined the soft state to be when HR $<$ 0.6, and the hard state when HR $\geq$ 0.6.

Second, we considered data only for days when simultaneous V- and H-band data were taken, as these data show the separate branches most clearly (we show all data as green points in Figure 6 for completeness). Using these criteria, we plotted in Figure 6 red data points when the HR $<$ 0.6 (soft state), black points when HR $\geq$ 0.6 (hard state), and blue points when the X-ray state could not be determined due to low X-ray flux. The analysis clearly shows that the bottom (red) branch corresponds to when GX 339-4 is in a soft X-ray state, while the top (black) branch corresonds to the hard X-ray state. Each branch represents a single-parameter family. Least-square linear fits were performed separately on each branch of data. The parameters of our best linear fits are recorded in Table 4.

3.1. Soft State

Our fits to the slope of the soft-state branch indicate that the flux increases more quickly at bluer wavelengths. In other words, the source gets bluer as it gets brighter. Figure 7 shows an example SED obtained from the soft-state branch data for $V = 16.0$ mag. The J, H and I-band data were extrapolated from the correlation data shown in Figure 5. The overall shape of the soft-state SED remains constant for V=17.5-16 mag (the magnitude range over which we have identified the soft-state branch), the only difference being that all four points move up in flux with increasing V-band mag. Here we investigate fitting thermal blackbody models to the SED to ascertain the flux source/s present during the soft-state.

We searched for appropriate fits by varying the temperature and outer radius of a blackbody. We assumed the mass of the black hole to be 10 M$\odot$ (Hynes et al. 2003), the binary inclination to be 15 or 80 deg (a parameter that is not well-established in GX 339-4 due to the lack of an observed ellipsoidal light curve or X-ray/optical eclipses), and the distance to the source to be either 6 or 15 kpc (Hynes et al. 2004; Zdziarski et al. 2004).

First we considered our data with respect to the Wein-tail limit of a very high-temperature blackbody ($T_{eff} = 1 \times 10^8$ K). Given the strength of the X-ray flux in this state, and the relatively small overall size of the system, irradiation of the outer disk might result in a high-temperature thermal source. We see that the V-, J-, H-band data can be explained by such a blackbody model, however, the I-band is discrepant (top panel, Figure 7), lying well below the curve. If we force the V- and I-band data to lie on the Wein-limit tail, the J- and H-band data lie well above the curve. Second, we considered a single-temperature blackbody fit of lower temperature. We were able to fit such a blackbody to the I-, J-, and H-band data, but not the V-band which lies significantly above the blackbody model (middle panel, .Figure 7). Third, we attempted to fit a multi-blackbody model that included two blackbodies, one of low-temperature, and the other high-temperature (an example is given in the bottom panel of Figure 7). We were unable to find a satisfactory fit to all four points as the slope between the I- and V-band data is too steep.

The results of our fits for the soft-state SED are given in Table 5. Figure 7 shows our fits for $i = 15$ deg and $d = 6$ kpc. The results summarized in the previous paragraph hold true for other values of i and d except for when $i = 80$ deg and $d = 15$ kpc. In this case we were unable to find any blackbody fit to the I, J or H-band data that had a radius within the tidal radius of GX 339-4 ($= 9.0 \times 10^{11}$ cm). Therefore, either the inclination or the distance is too high in this case.

3.2. Hard-state

In contrast to the soft state, the O/IR flux in the hard state becomes redder with increasing flux. This requires either a non-thermal source or a thermal source that dramatically increases in size as it decreases in temperature. In this section we first explore whether thermal-only models can explain the hard-state SED, as done for the soft-state SED in Section 3.1. Then we compare our O/IR SED to simultaneous radio data and investigate how non-thermal models may describe the data.

Since the hard-state SED at other V-band magnitudes exhibits a similar shape to that seen at $V = 15.14$ mag, we focussed our model-fitting efforts to this one SED. This V-band magnitude was chosen as it was the magnitude observed during simultaenous radio observations in 2002 (see below). Using the same method as for the soft-state SED, we fitted 1) a single, very-high temperature blackbody; 2) a single, low-temperature blackbody; and 3) a combination of the two, to the hard-state SED. Example fits are given in Figure 8. In the single high-temperature blackbody case, only the V and I-band data can be explained by such a model. The J- and H-band data lie significantly above. When attempting to fit the low-temperature blackbodies we were unable to find any thermal blackbody that had an outer radius less than the tidal radius of GX 339-4 for any given combination of i and d.

The hard state is known to be correlated with radio emission, presumably due to synchrotron emission from a jet (Fender 2001, Belloni; Gallo et al. 2004; Corbel & Fender 2002; Corbel et al. 2003). It is plausible that such emission might contribute significantly at near-IR bandpasses. In such a case, a power-law source consistent with the radio plus a UV-bright thermal source similar to the first thermal source in the soft state may explain the hard state O/IR flux.

We searched the literature for radio observations that were taken on the same night as our SMARTS data during the hard state. We found one case of radio observations taken

on UT 18 April 2002 (Gallo et al. 2004) in two radio bands: 8640 MHz (13.49 ± 0.08 mJy) and 4800 MHz (12.97 ± 0.07 mJy). On this date, GX 339-4 had a V-band magnitude of 15.14 mag. We show this radio data along with our O/IR hard-state SED in Figure 9. If we fit a power-law to the two radio points and extend it to O/IR wavelengths, it lies well beneath the O/IR fluxes (short-dashed line in Figure 9). A straight-line fit to the radio + O/IR data (long-dashed line) shows that the I-band data is inconsistent with such a non-thermal model and does not go through the radio data (including the small errors). If we fit a straight-line to radio + IR data only (dot-dashed line), we don't see much change of the fit through the radio data in that, again, the I-band data cannot be explained by such a model. However, the V-, J-, and H-band data can be.

In conclusion, we find that the hard-state SED cannot be explained solely by thermal models or non-thermal models. It seems that the SED needs to be explained by a combination of thermal and non-thermal models. We are unable to perform such a fit since the number of parameters involved would exceed the number of data points available. This highlights the need to obtain simultaneous data at other wavelengths, such as B, UV, and mid-IR to further sample the shape of the SED near the O/IR and to constrain such model fits.

3.3. Timing

We have calculated the power spectral density (PSD) of the variability of GX 339-4 in the hard and soft states. The PSD corresponds to the power in the variability of emission as a function of timescale. We divide the the H- and V-band light curves into "hard" and "soft" intervals, respectively, based on the hardness ratio in the contemporaneous RXTE-PCA observations, as outlined in Section 3. We calculated the PSDs of the V (JD = 2453224.70 - 2453478.79) and H-band (JD = 2454498.88 - 2454746.55) light curves. These

two bands were chosen as the H-band data shows light-curve variability most clearly during the hard-state, while the same is true for the V-band during the soft state. However, PSDs were calculated for each band in both the hard- and soft-states. The time intervals chosen were the longest well-sampled intervals during which the X-ray hardness ratio stayed soft and hard, respectively.

The raw PSD calculated from a light curve combines two aspects of the dataset: (1) the intrinsic variation of the object and (2) the effects of the temporal sampling pattern of the observations. In order to remove the latter, we apply a Monte-Carlo type algorithm based on the "Power Spectrum Response Method" (PSRESP) of Uttley, McHardy, & Papadakis (2002) to determine the intrinsic PSD (and its associated uncertainties) of the light curves. Our realization of PSRESP is described in Chatterjee et al. (2008). PSRESP gives both the best-fit PSD model and a "success fraction" $F_{\rm succ}$ (fraction of simulated light curves that successfully represent the observed light curve) that indicates the goodness of fit of the model. We bin the data in 1 to 2-day time intervals, averaging all data points within each bin to calculate the flux. We filled empty bins through linear interpolation of the adjacent bins in order to avoid gaps that would distort the PSD. We accounted for the effects of the binning and interpolation by inserting in each of the simulated light curves the same gaps as occur in the actual data and performing the same binning and interpolation procedures.

In Figure 10 we show the PSDs of GX 339-4 and the best-fit model in H- (hard state) and V-bands (soft state). The PSDs show red noise behavior, i.e., there is higher amplitude variability on longer than on shorter timescales. Based on the model with the highest success fraction, the H-band PSDs, and therefore the hard-state PSDs, is best fit with a simple power law of slope $-1.8^{+0.3}_{-0.7}$, for which the success fraction is 0.56. That for the V-band (soft state) PSD is $-2.0^{+0.3}_{-0.5}$ with success fraction 0.89. During the fitting, we varied the slope from -1.0 to -3.0 in steps of 0.1. The uncertainties of the slopes represent the

range of slopes beyond which the success fraction goes below half of the maximum value. The rejection confidence, equal to one minus the success fraction, is much less than 0.9 in both cases. This implies that a simple power-law model provides an acceptable fit to the PSD at both wavebands. PSDs for the V band during the hard state, and H-band during the soft state, were also well-fitted by a simple power law model with slopes consistent with those described here within uncertainties. A summary of our PSD fits are given in Table 6.

We see no evidence of any specific timescale in the hard or soft state variability, such as a break in the power spectra, at few days to few months timescales. We defer a discussion of timescales smaller than a few days, which necessarily involves observations with denser sampling, to future work.

4. Discussion and Conclusions

We have presented a comprehensive optical and near-infrared light curve of GX 339-4 between 2002 and 2010, inclusive. The light curve shows that GX 339-4 is continuously in outburst (that is, the companion star never dominates the O/IR flux) but experiences significant changes in luminosity and spectral state.

We have found strong correlations within the O/IR with two branches corresponding to either the hard or soft X-ray states. These correlations are similar to those seen between O/IR and X-ray flux (Coriat et al. 2009) with distinct branches corresponding to the hard and soft states, and an apparent change in slope of the hard-state branch. With the correlations so clearly defined, particularly between V- and H-band, it is possible to define in which state GX 339-4 resides from the O/IR data alone.

Both the soft- and hard-state show evidence of multi-component flux sources in the O/IR. During the soft-state, the O/IR SED is consistent with a multi-thermal flux source

model, where one thermal source is of very high temperature and the other with a lower temperature. This conclusion rests somewhat on the fact that the I-band data seems "discrepant" from the other three bands. If we assume the I-band data should lie on a straight line with the V, J, and H-band data, then the I-band would need to move up by 0.25 dex in the soft-state SED (0.35 dex in the hard-state SED). Our investigation of our flux calibration (Section 2.4) method showed that the largest deviation between our observations and the published fluxes was 0.05 dex in log(flux) space. We checked our magnitude calibration by searching the literature for simultaneous multiwavelength observations of GX 339-4 taken by other investigators to see if their I-band data agree with ours for a given V-band magnitude in a particular X-ray state. Only one case was found of multiwavelength observations. Optical data was taken on UT 1981 May 28 (Motch, Ilovaisky, & Chevalier 1981) when GX 339-4 was in a hard-state, with the following results: $V = 15.4$, $I = 13.9$ ($B = 16.2$, $R = 14.8$). Given this V-band magnitude, we calculated $I = 13.97$ mag from our hard-state correlation data, a difference of only 0.07 mag from that observed by Motch, Ilovaisky, & Chevalier (1981). We are therefore confident that our magnitude calibration is correct. Taking the higher of the two color-corrections (Section 2.1.2) translates into a difference in the I-band flux of 0.06 dex in log(flux) space. This, along with any flux-calibration error, accounts for no more than ~ 0.11 dex, much less than what would be required for the I-band to be "aligned" with the other three bands. Therefore we believe the change in flux between the V-I-J bands is real and provides evidence of multiple flux sources in this region of the O/IR spectrum.

The hard-state SED show no satisfactory fits of either a purely non-thermal or multi-thermal emission models, and we are unable to perform fits of a non-thermal + thermal model due to the lack of data. More sophisticated model-fits of the hard-state SED have been performed by Markoff et al. (2005) and Maitra et al. (2009). Markoff et al. (2005) included data from the radio and X-ray regimes, and used quasi-simultaneous O/IR

data in 1981 obtained by Motch, Ilovaisky, & Chevalier (1981) and Pederson (1981). Their conclusions were that the O/IR could be explained by a combination of a multi-temperature Shakura & Sunyaev (1973) disk and a single-temperature blackbody representing the irradiation of the outer accretion disk by the jet, with the IR dominated by flux from a jet. The temperature of the single-blackbody was required to be T$\sim 5 \times 10^4$ K. Maitra et al. (2009) used 2002 hard-state O/IR, radio and X-ray data when fitting their models and found that the SED could be entirely explained by a jet-only model. However, the O/IR region was only sampled by three points (Homan et al. 2005, V-, I-, and H-band), whereas the 1981 dataset used by Markoff et al. (2005) included 9 data points from B to the mid-IR. Had data at shorter wavelengths been available, Maitra et al. may have seen evidence for higher flux at shorter wavelengths, which may pose problems for a jet-only model fit. At the very least, their model does not go through the H-band data. In our opinion, we feel there is room for doubt on a jet-only model when it comes to explaining the O/IR SED of GX 339-4 during the hard state. This, and other studies, highlight the importance of obtaining simultaeneous, multiwavelength data, particularly in the O/IR where the contribution by multiple flux sources is significant, thereby presenting crucial limits on any theoretical models. For this reason, a greater wavelength range sampled in the O/IR is required and we encourage future multiwavelength studies to include data at UV, B, and mid-IR wavelengths in addition to the optical, radio and X-ray data usually obtained.

Timing analysis during the soft-state (V-band) and hard-state (H-band) show the variability of GX 339-4 is consistent with a power-law over timescales 4-230 days. Gandhi (2009) produced a PSD of GX 339-4 during the hard-state (albeit when the optical counterpart was faint) for timescales 0.17-250 secs and detected a peak at 0.05 Hz (20 secs) that was not detected in the accompanying X-ray PSD. Future timing studies should try to bridge the timescale-gap between 250 secs and 4 days to fully explore the variability

timescales in GX 339-4 in an attempt to see any evidence of accretion-related processes.

We will continue to monitor GX 339-4 in the O/IR with SMARTS for the foreseable future, including data at B-, V-, I-, J- H-, and K-bands, making it immediately public via the web for use by the general astronomical community.

We are grateful to our SMARTS ANDICAM observers, Juan Espinoza, Alberto Miranda, and David Gonzalez, and to Suzanne Tourtellotte for reducing the optical data.

MMB, CDB, HC, and RC are supported by NSF/AST grants 0407063 and 070707 to CDB.

J.A.T. acknowledges partial support from the Suzaku Guest Observer grant NNX09AG46G.

EK and TD acknowledge TUBITAK grant 106T570, Turkish Academy of Sciences and the EU FP7, ITN 215212 "Black Hole Universe".

This research has made use of the NASA/ IPAC Infrared Science Archive, which is operated by the Jet Propulsion Laboratory, California Institute of Technology, under contract with the National Aeronautics and Space Administration.

Facilities: CTIO SMARTS (1.3m).

REFERENCES

Bailyn, C.D. & Ferrara, L. 2004, ATel No. 323

Bessell, M.S. 1990, PASP, 102, 1181

Bessell, M.S., Castelli, F., & Plez, B. 1998, A&A, 333, 231

Buxton, M., & Vennes, S. 2003, MNRAS, 342, 105

Buxton, M., & Bailyn, C.D. 2004, ApJ, 615, 880

Casella, P. et al. 2006, MNRAS, 404, L21

Cannizzo, J.K., Chen, W., & Livio, M. 1995, ApJ, 454, 880

Cannizzo, J.K., & Mattei, J.A. 1998, ApJ, 505, 344

Cardelli, J.A., Clayton, G.C., & Mathis, J.S. 1989, ApJ, 345, 245

Chatterjee, R. et al. 2008, ApJ, 689, 79

Chen, W., Shrader, C.R., & Livio, M. 1997, ApJ, 491, 312

Corbel, S., & Fender, R.P. 2002, ApJ, 573, 35

Corbel, S., Nowak, M.A., Fender, R.P., Tzioumis, A.K., & Markoff, S. 2003, A&A, 400, 1007

Coriat, M., Corbel, S., Buxton, M.M., Bailyn, C.D., Tomsick, J.A., Kording, E., & Kalemci, E. 2009, MNRAS, 400, 123

DePoy, D.L., et al. 2003, SPIE, 4841, 827

Dubus, G., Lasota, J.-P., Hameury, J.-M., & Charles, P. 1999, MNRAS, 303, 139

Dubus, G., Jameury, J.-M., & Lasota, J.-P. 2001, A&A, 373, 251

Elias, J.H., Frogel, J.A., Matthews, K., & Neugebauer, G. 1982, AJ, 87, 1029

Fender, R.P. 2001, MNRAS, 322, 31

Fender, R.P., Belloni, T.M., & Gallo, E. 2004, MNRAS, 355, 1105

Frogel, J.A., Persson, S.E., Aaronson, M., & Matthews, K. 1978, ApJ, 220, 75

Gallo, E., Corbel, S., Fender, R.P., Maccarone, T.J., & Tzioumis, A.K. 2004, MNRAS, 347, L52

Gandhi, P. et al. 2008, MNRAS, 390, L29

Gandhi, P. 2009, ApJ, 697, L167

Gandhi, P. et al. 2010, MNRAS, 407, 2166

Hamuy, M. et al. 1992, PASP, 104, 533

Hamuy, M. et al. 1994, PASP, 106, 566

Homan, J., Buxton, M., Markoff, S., Bailyn, C., Nespoli, E., & Belloni, T. 2005, ApJ, 624, 295

Hynes, R.I., Steeghs, D., Casares, J., Charles, P.A., & O'Brien, K. 2003, ApJ, 583, L95

Hynes, R.I., Steeghs, D., Casares, J., Charles, P.A., & O'Brien, K. 2003, ApJ, 609, 317

Jain, R.K., Bailyn, C.D., Orosz, J.A., McClintock, J.E., & Remillard, R.A. 2001, ApJ, 554, L181

Landolt, A.U. 1992, AJ, 104, 340L

Lasota, J-P 2001, NewAR, 45, 449

Maitra, D., & Bailyn, C.D. 2008, ApJ, 688, 537

Maitra, D., Markoff, S., Brocksopp, C., Noble, M., Nowak, M., & Wilms, J. 2009, MNRAS, 398, 1638

Markoff, S., Nowak, M., Corbel, S., Fender, R., and Falcke, H. 2005, A&A, 397, 645

Motch, C., Ilovaisky, S.A., & Chevalier, C. 1981, IAU Circ. 3609

Neil, E.T., Bailyn, C.D., & Cobb, B.E. 2007, ApJ, 657, 409

Pederson, H. 1981, IAU Circ. 3613

Persson, S.E., Murphy, D.C., Krzeminski, W., Roth, M., & Rieke, M.J. 1998, AJ, 116, 2475

Remillard, R.A., & McClintock, J.E. 2006, ARA&A, 44, 49

Shakura, N.I., & Sunyaev, R.A. 1973, A&A, 24, 337

Subasavage, J.P. et al. 2010, SPIE, 7737, 31

Uttley, P., McHardy, I.M., & Papadakis, I.E. 2002, MNRAS, 332, 231

Wu, K., Soria, R., Hunstead, R.W., & Johnston, H.M. 2001, MNRAS, 320, 177

Zdziarski, A.A., Poutanen, J., Mikolajewska, J., Gierlinski, M., Ebisawa, K., & Johnson, W.N. 1998, MNRAS, 301, 435

Zdziarski, A.A. et al. (2004), MNRAS, 351, 791

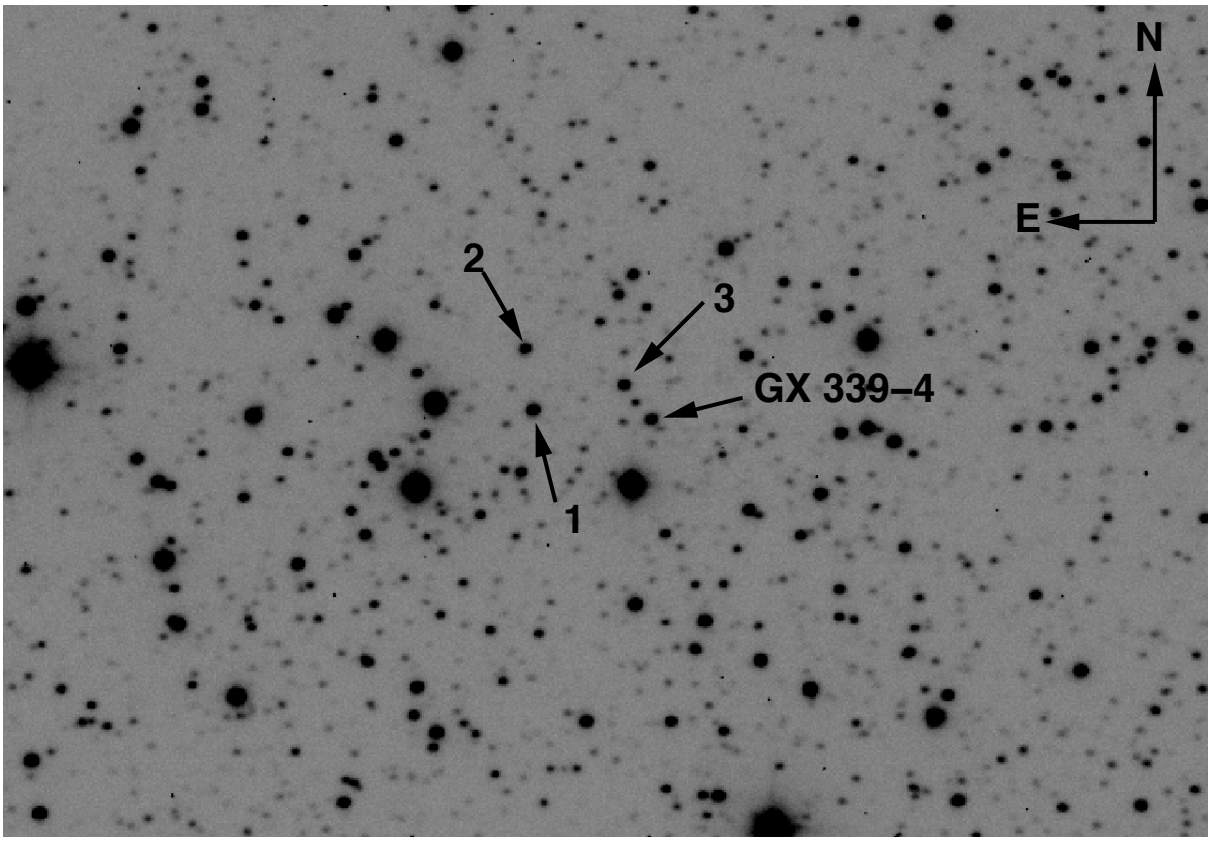

Fig. 1.— V-band finding chart for GX 339-4. Field of view is 3.7' x 2.7'.

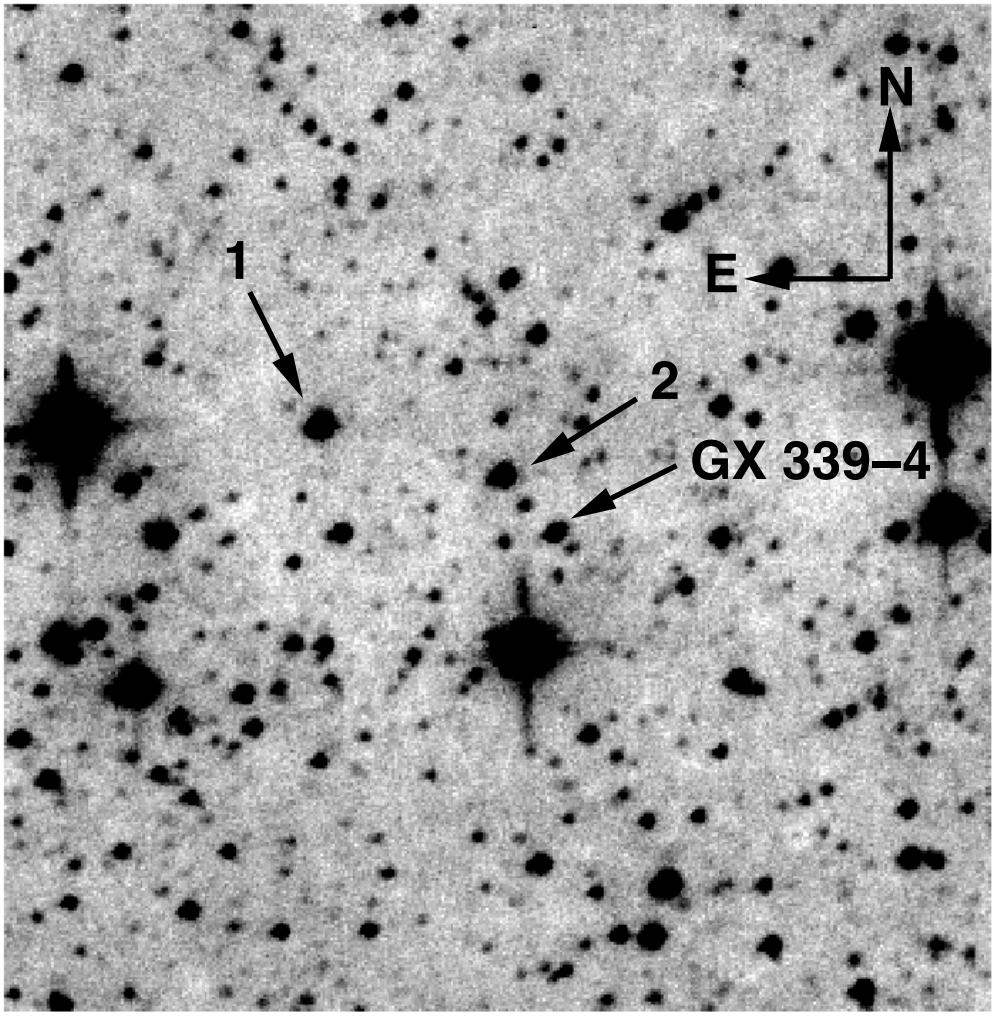

Fig. 2.— H-band finding chart, field size is 2.4' x 2.4'

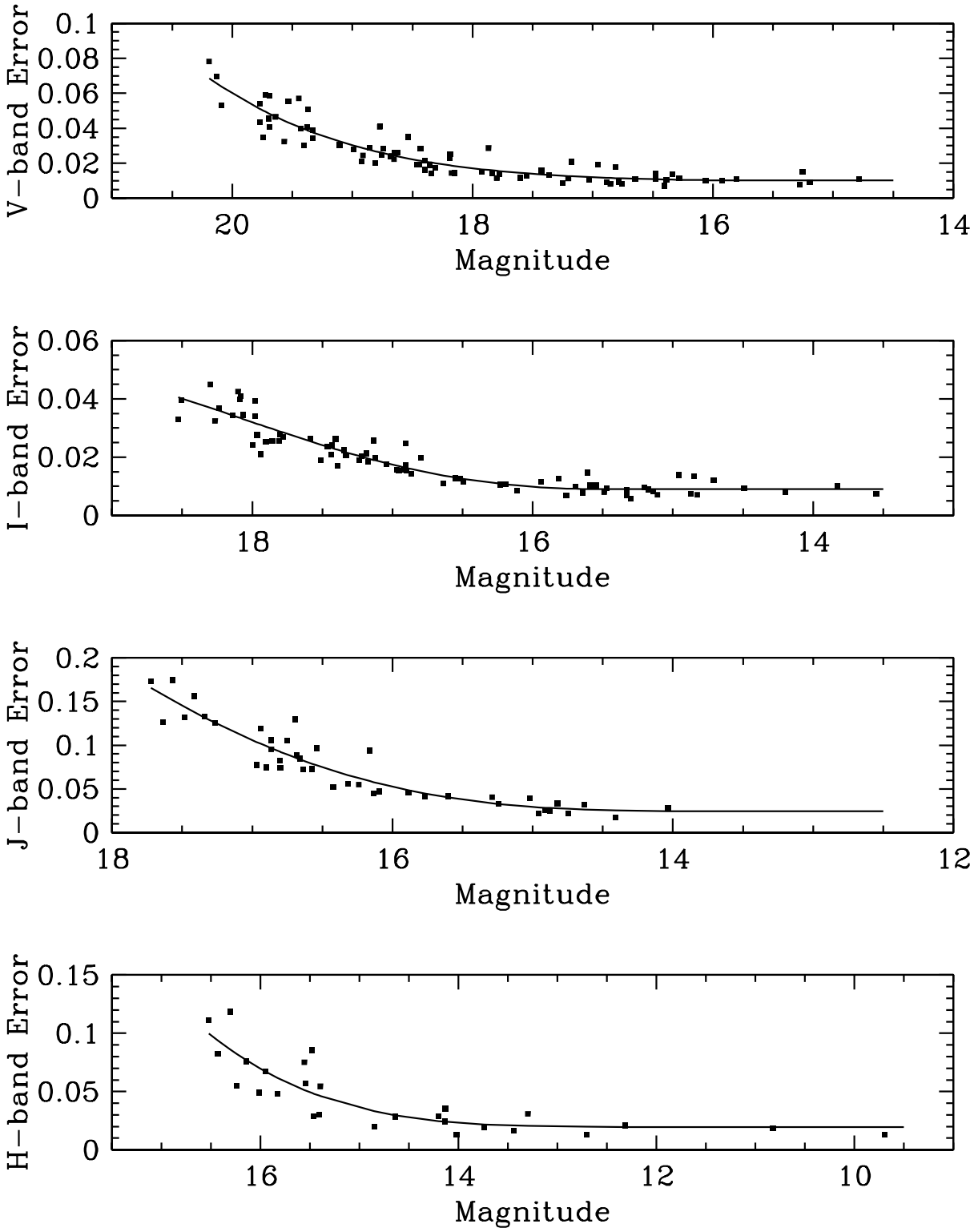

Fig. 3.— Photometric error of stars in the GX 339-4 field versus magnitude for optical and near-infrared bands. The solid line is a 4th-order polynomial fit. The y-axis is the 1-σ dispersion of measurements of stars over 93 nights as described in Section 2.1.3.

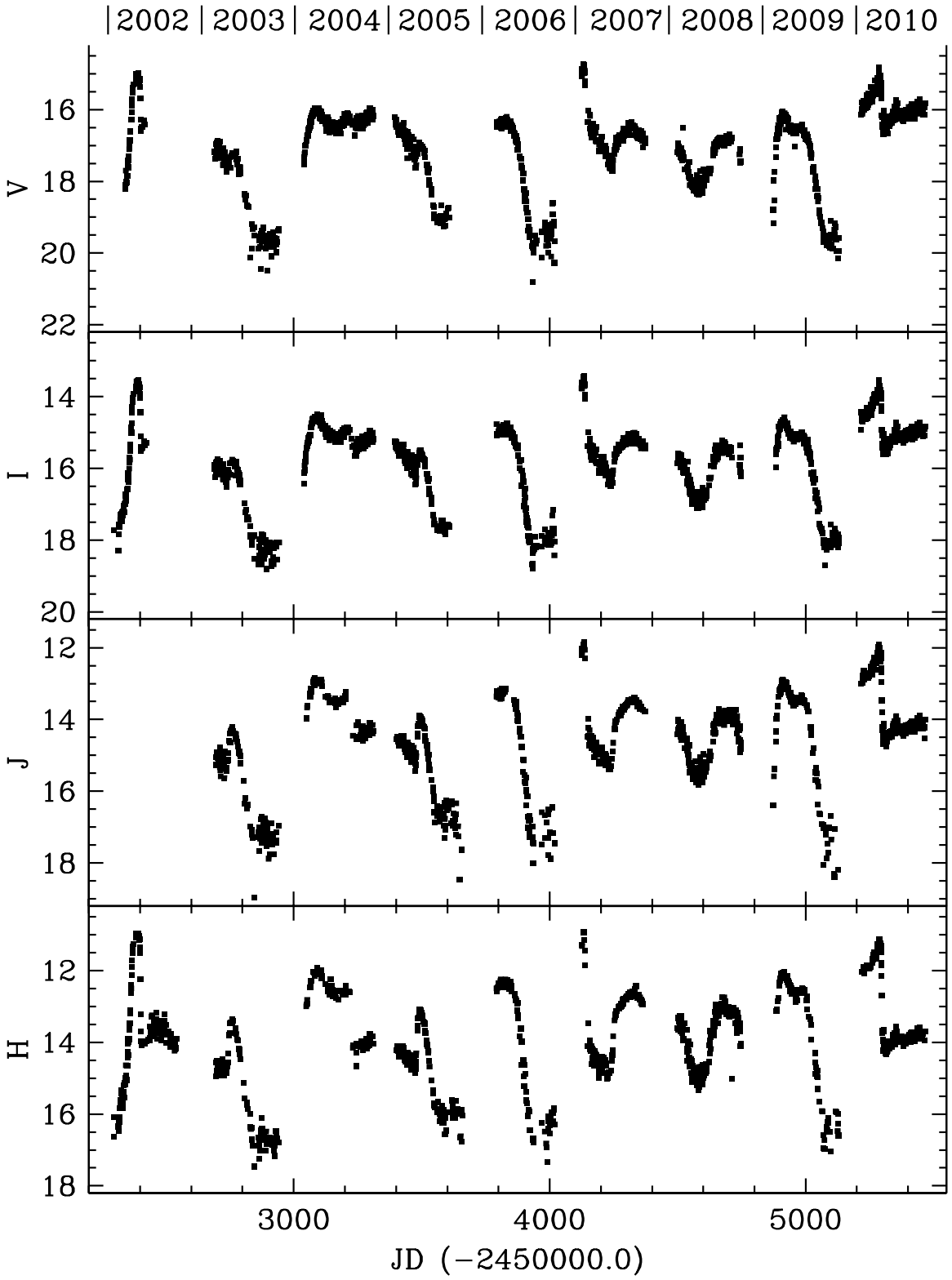

Fig. 4.— The SMARTS 1.3m optical and near-infrared light curve of GX 339-4 during 2002-2010, inclusive.

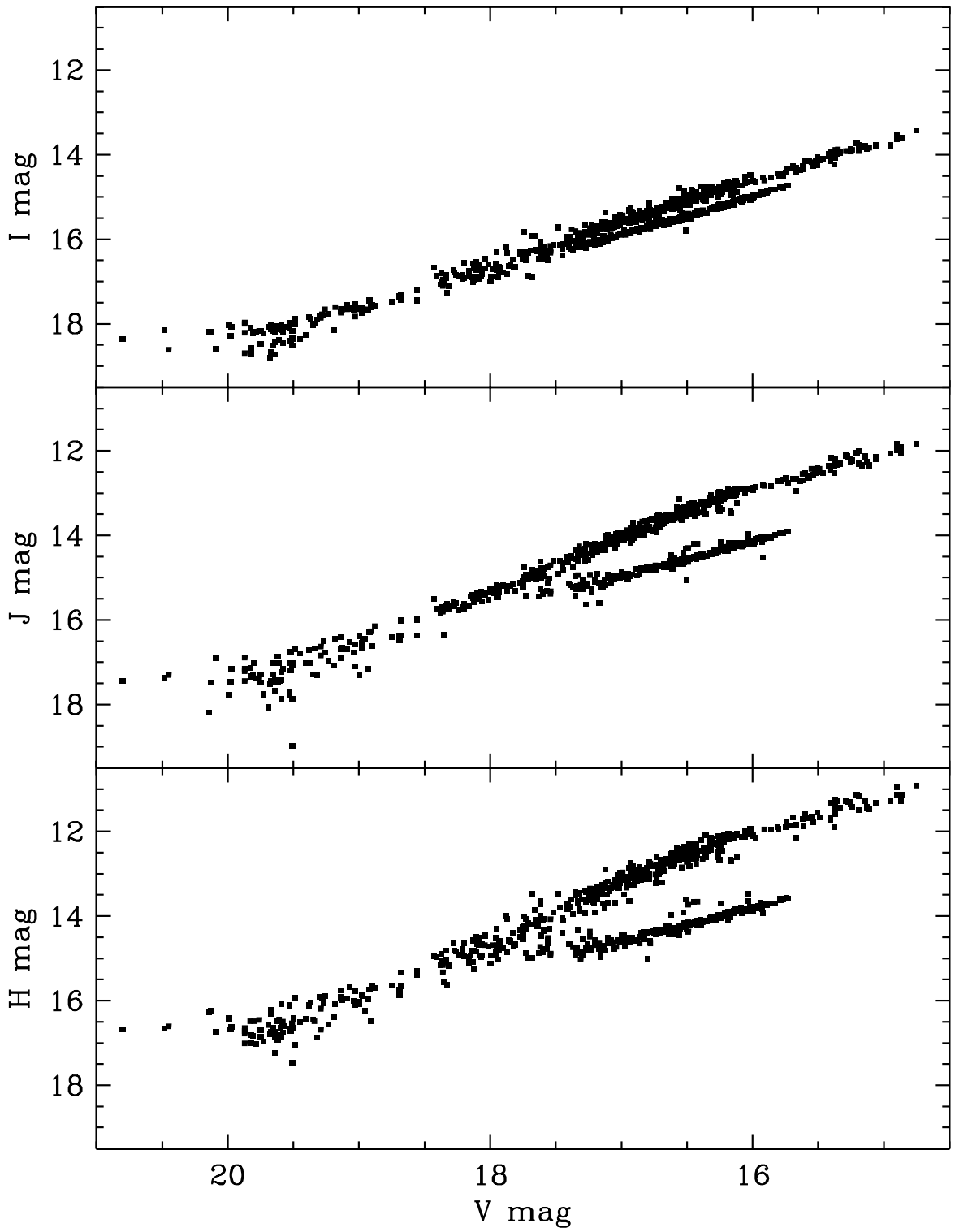

Fig. 5.— Correlations between the V-band magnitudes and (top) I-band, (middle) J-band, and (bottom) H-band magnitudes.

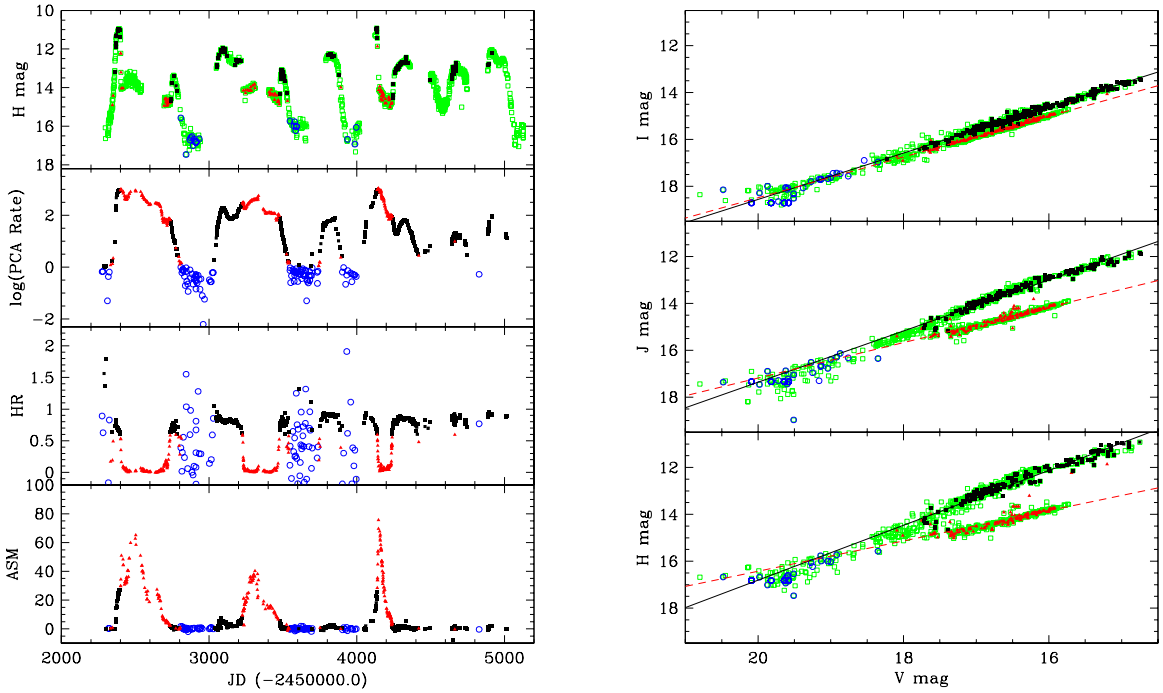

Fig. 6.— *Left*: H-band light curve and RXTE data. We categorized hard/soft state H-band data only for days when we had simultaneous RXTE data, else the data is shown as green open squares. Black solid squares corresponds to days when the hardness ratio is ≥ 0.6 (hard state) and red solid triangles when the hardness ratio is < 0.6 (soft state). Data for which the PCA count rate is < 1.0 count/sec was not cateogrized and is shown as blue open circles. *Right*: Data are represented using the same criterion as the left figure, and categorized into hard and soft states only for days when there were simultaneous RXTE data. The lines are linear fits whose parameters are given in Table 4.

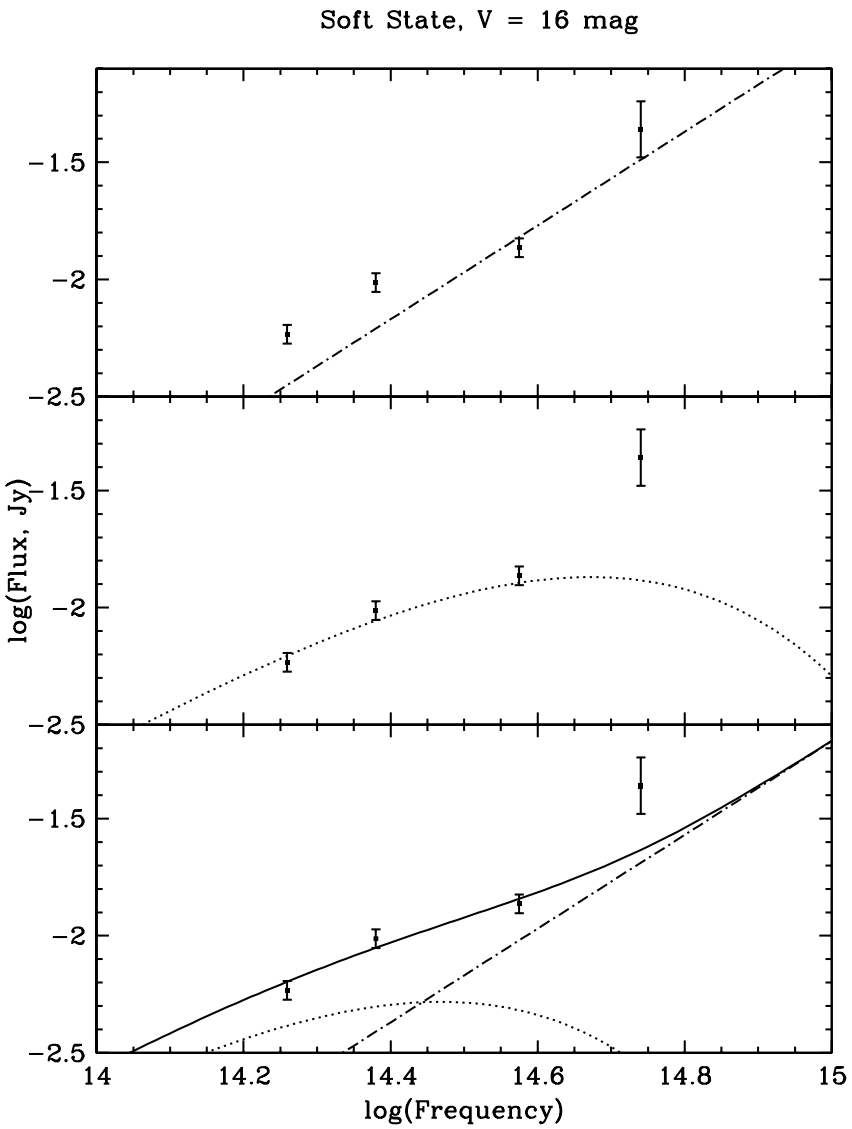

Fig. 7.— Soft-state SED of GX 339-4 for V = 16 mag. $I-, J$-, and H-band data were extrapolated from the correlations shown in Figure 5. The errors are the combined photometric and redenning errors as outlined in Section 2.4. *Top*: Line is the Wein-tail limit of a high-temperature blackbody, fit to V and I-band data. *Middle*: Dotted line is a single-temperature blackbody of T_{eff} = 8000 K and $R_{out} = 2.8 \times 10^{11}$ cm; *Bottom*: Dotted line is a single-temperature blackbody of T_{eff} = 5000 K and $R_{out} = 3.5 \times 10^{11}$ cm, dot-dashed line is Wein-tail limit of a $T_{eff} = 1 \times 10^8$ K temperature blackbody, solid line is combined model of the two. In all cases, the slope between the V and I-band data is too steep to be explained by either a single- or multi-temperature blackbody model. All fits were done for i = 15 deg, and d = 6 kpc. Results for other combinations of i and d can be found in Table 5.

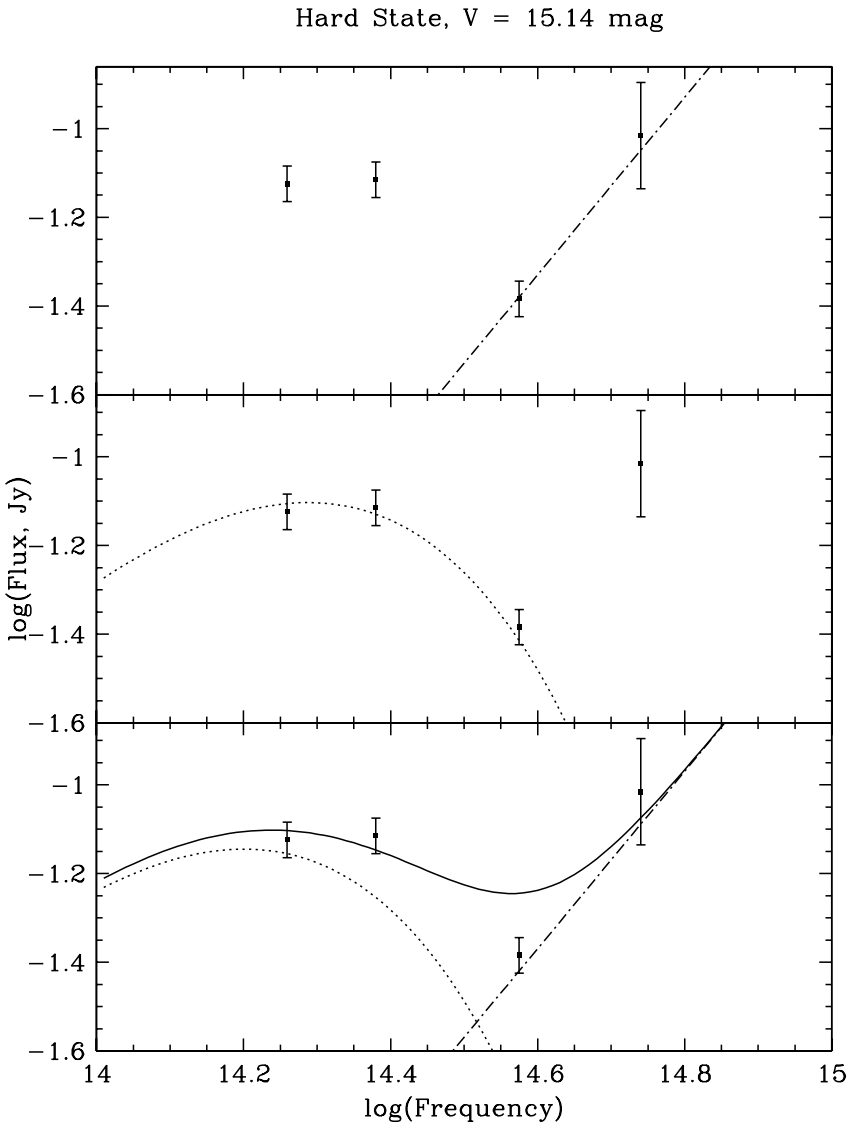

Fig. 8.— As for Figure 7 but for the hard-state for $V = 15.14$ mag. *Top*: Line is the Wein-tail limit of a high-temperature blackbody, fit to V and I-band data only. *Middle*: Dotted line is a single-temperature blackbody of $T_{eff} = 3300$ K and $R_{out} = 2.6 \times 10^{12}$cm. Note that this is unphysical since it would extend beyond the tidal radius of GX 339-4 ($= 9.0 \times 10^8$ cm); *Bottom*: Dotted line is a single-temperature blackbody of $T_{eff} = 2700$ K and $R_{out} = 3.3 \times 10^{12}$ cm which would extend beyond the tidal radius. The dot-dashed line is the Wein-tail limit of a $T_{eff} = 1 \times 10^8$ K temperature blackbody, and the solid line is the combined model of the two. All fits were done for $i = 15$ deg, and $d = 6$ kpc. The hard-state SED cannot be explained by thermal models alone.

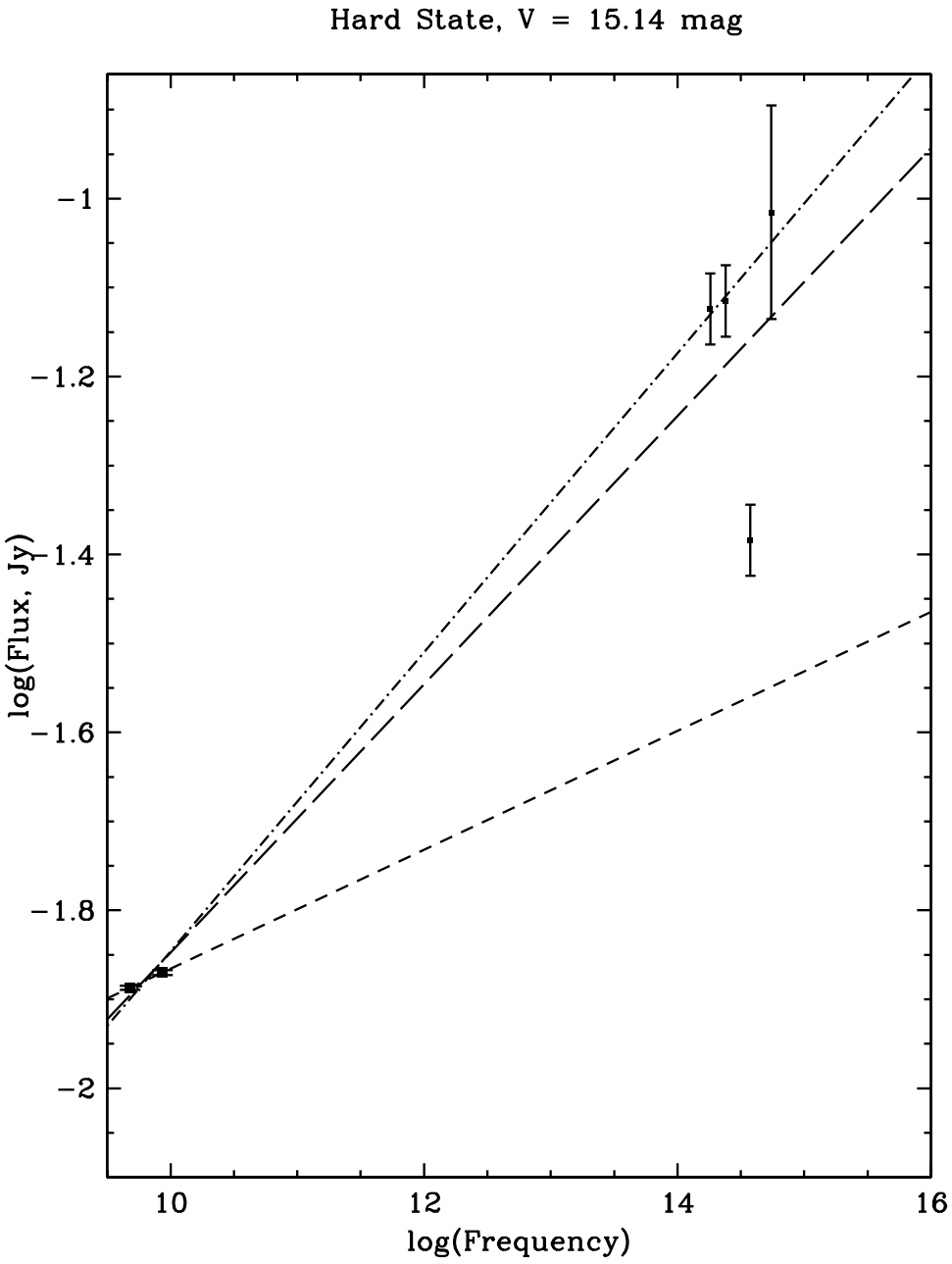

Fig. 9.— Multi-component model fits to the hard-state spectral energy distribution for V = 15.14, when simultaneous O/IR and radio data were obtained on UT 18 April 2002. Lines are the non-thermal model-fits to radio data only (short-dashed line), radio + O/IR data (long-dashed line), and radio+IR data (dot-dashed line). The O/IR data are not consistent with a non-thermal model fitted only to the radio data, but the radio + IR data may be consistent with a non-thermal model.

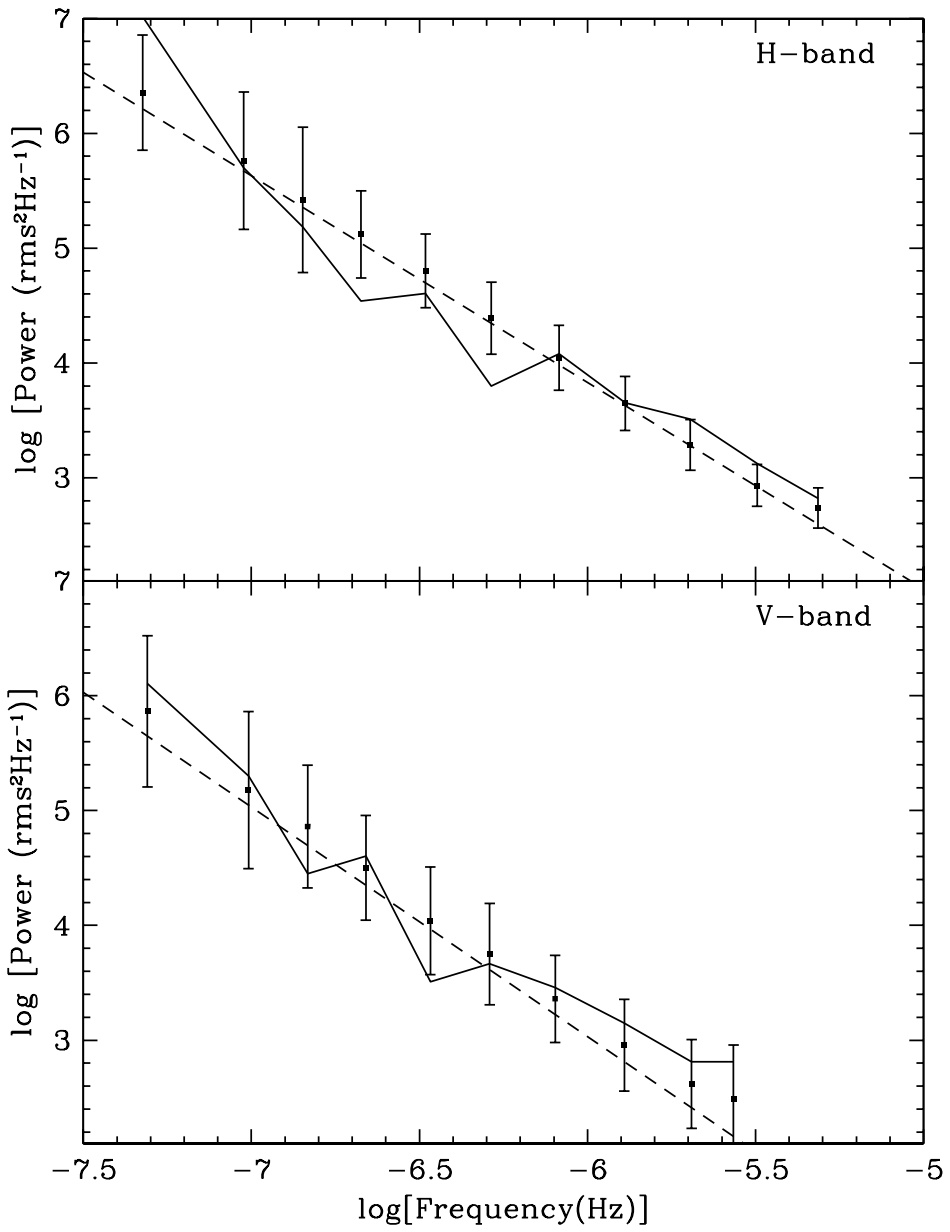

Fig. 10.— Power spectral densities of the hard state H-band, and soft state V-band, light curves. The PSD of the observed data is shown by the solid jagged line, while the underlying power-law model is shown by the dashed straight line. Points with error bars correspond to the mean value of the PSD simulated from the underlying power-law model. The error bars are the standard deviation of the distribution of simulated PSDs. The broadband power spectral density is best described by a simple power law with a slope −1.8 at H-band, and −2.0 at V-band. See Table 6 for the PSD fit results for the V-band during the hard state and H-band during the soft state.

Table 1. Optical comparison star magnitudes.

Number	RA (J2000.0)	Dec (J2000.0)	V (mag)	I (mag)	$(V-I)$ (mag)
1	17:02:51.8	-48:47:21.8	16.99 ± 0.05	15.62 ± 0.06	1.37
2	17:02:52.0	-48:47:09.5	17.54 ± 0.06	15.26 ± 0.07	2.28
3	17:02:49.9	-48:47:17.1	17.43 ± 0.05	15.49 ± 0.07	1.94

Note. — Star numbers are in accordance with the optical finding chart (Figure 1).

Table 2. Near-infrared comparison star magnitudes.

Number	RA (J2000.0)	Dec (J2000.0)	J (mag)	H (mag)
1	17:02:52.0	-48:47:09.5	13.35 ± 0.09	12.49 ± 0.09
2	17:02:49.9	-48:47:17.1	13.88 ± 0.09	13.02 ± 0.10

Note. — Star numbers are in accordance with the IR finding chart (Figure 2).

Table 3. Calibrated V-, I-, J-, and H-band magnitudes, fluxes and their errors of GX 339-4 from 2002 - 2010, inclusive (abbreviated). The JD is that at the start of the observing sequence. The full version can be accessed online.

year	JD (-2450000.0)	V mag (mag)	V err (mag)	V_0 flux (Jy)	V_0 err (Jy)	I mag (mag)	I err (mag)	I_0 flux (Jy)	I_0 err (Jy)	J mag (mag)	J err (mag)	J_0 flux (Jy)	J_0 err (Jy)	H mag (mag)	H err (mag)	H_0 flux (Jy)	H_0 err (Jy)
2002	2297.85400	-	-	-	-	17.730	0.030	0.00103	0.00003	-	-	-	-	16.080	0.070	0.00069	0.00005
	2298.87070	-	-	-	-	-	-	-	-	-	-	-	-	16.640	0.110	0.00041	0.00004
	2314.84330	-	-	-	-	18.280	0.040	0.00062	0.00002	-	-	-	-	16.360	0.090	0.00053	0.00005
	2314.84830	-	-	-	-	-	-	-	-	-	-	-	-	16.340	0.090	0.00054	0.00005
	2316.83520	-	-	-	-	-	-	-	-	-	-	-	-	16.480	0.100	0.00048	0.00005
	2317.84150	-	-	-	-	17.840	0.030	0.00093	0.00003	-	-	-	-	16.470	0.100	0.00048	0.00005
	2318.81040	-	-	-	-	17.630	0.030	0.00112	0.00003	-	-	-	-	15.830	0.060	0.00087	0.00005
	2319.85140	-	-	-	-	17.570	0.030	0.00119	0.00003	-	-	-	-	16.210	0.080	0.00061	0.00005
	2320.83940	-	-	-	-	17.600	0.030	0.00116	0.00003	-	-	-	-	16.090	0.070	0.00068	0.00005
	2322.86770	-	-	-	-	17.440	0.020	0.00134	0.00002	-	-	-	-	15.710	0.060	0.00097	0.00006

Table 4. Best-fit straight-line parameters to O/IR correlations.

Data/Branch	Slope	y-axis Intercept
V/I hard	0.988	-1.206
V/J hard	1.093	-4.490
V/H hard	1.170	-6.592
V/I soft	0.869	1.111
V/J soft	0.756	2.060
V/H soft	0.645	3.514

Table 5. SED fit results for GX 339-4 during the soft state when $V = 16$ mag. The temperatures and outer radii shown are given for the low-temperature blackbody only. The high-temperature blackbody model had $T_{eff} = 1 \times 10^8$ K, with the outer radius adjusted to fit the data. Note that the fits found for $i = 80$ deg and $d = 15$ kpc give radii that extend beyond the tidal radius of GX 339-4 ($= 9.0 \times 10^{11}$ cm).

Model Fit	Distance (kpc)	Inclination (deg)	T_{eff} (Kelvin)	R_{out} (cm)
Single, low-temp	6	15	8000	2.8×10^{11}
	15	15	8000	7.0×10^{11}
	6	80	8000	6.7×10^{11}
	15	80	8000	2.6×10^{12}
Multi, low+high temp	6	15	5000	3.5×10^{11}
	15	15	5000	8.9×10^{11}
	6	80	5000	8.1×10^{11}
	15	80	5000	3.5×10^{12}

Table 6. A summary of the best-fit power-law parameters to the power spectral densities of GX 339-4 during the hard and soft states.

Filter/X-ray state	Start JD	End JD	Slope (α)
V soft state	3224.70050	3478.79434	$-2.0^{+0.3}_{-0.5}$
V hard state	4498.88162	4746.54995	$-1.8^{+0.3}_{-0.5}$
H soft state	3224.70050	3478.79434	$-1.7^{+0.2}_{-0.6}$
H hard state	4498.88162	4746.54995	$-1.8^{+0.3}_{-0.7}$